Supplementary data

Active Site Engineering of Fe- and Ni-sites for Highly Efficient Electrochemical Overall Water Splitting

Lejuan Cai, Bocheng Qiu, Ziyuan Lin, Yang Wang, Sainan Ma, Mengye Wang, Yuen Hong Tsang and Yang Chai*

Department of Applied Physics, The Hong Kong Polytechnic University, Hung Hom, Kowloon, Hong Kong, People's Republic of China

*To whom the correspondence should be addressed: y.chai@polyu.edu.hk

Experimental section

Synthesis and Preparation: Fe-doped Ni_2P was synthesized directly onto SS mesh using a chemical bath deposition technique followed by phosphorization process. $Ni(NO_3)_2 \cdot 6H_2O$ (1.454 g) and NH_4NO_3 (0.2 g) were added into 35 mL of de-ionized water. Then 5 mL of 28 wt% ammonia was added into the green solution and formed dark blue nickel ammonia complex. After stirring in air for 10 min, the solution was poured into a round-bottom flask and pre-heated at 85° C for 1 h. Meanwhile, a stainless steel (SS) mesh was sequentially cleaned in isopropanol, acetone and de-ionized water, and treated with 10% HCl for 10 min before rinsed with DI water. Next, the SS was placed into the pre-heated nickel ammonia and the flask were kept at 85° C for different time duration to obtain Fe-doped $Ni(OH)_2$/SS. The iron in Fe-doped $Ni(OH)_2$/SS was derived from the substitutional reaction between $[Ni(NH_3)_6]^{2+}$ and iron in SS mesh. The $Ni(OH)_2$-HF and $Ni(OH)_2$-LF were prepared after one-hour and three-hour deposition time, respectively.

To prepare Fe-doped Ni_2P/SS, Fe-doped $Ni(OH)_2$/SS and 0.5 g NaH_2PO_2 were put in a quartz boat and NaH_2PO_2 was placed at the upstream. Subsequently, the quartz boat was transferred into a tube furnace. The heating center temperature of the furnace was raised up to 300 °C with the heating rate of 5 °C/min and held at this temperature for 120 min in an Ar flow with a flow rate of 20 sccm. The obtained Fe-doped Ni_2P on SS mesh derived from $Ni(OH)_2$-HF and $Ni(OH)_2$-LF were denoted Ni_2P-HF and Ni_2P-LF, respectively.

Electrochemical Tests: A three electrodes electrochemical station was used to test electrochemical performance (CHI 660D). All electrochemical tests were performed in 50 mL of 1.0 M KOH electrolyte (pH = 14.0). The prepared sample, Hg/HgO and graphite rod were applied as working electrode, reference electrode and counter electrode, respectively. The performance of the OER was tested using linear sweep voltammetry (LSV) with a scanning window of 1.2 V to 1.6 V vs RHE and a scan rate of 2 mV s^{-1}. The performance of the HER was tested using linear sweep voltammetry (LSV) with a scanning window of 0 V to -0.6 V vs RHE and a scan rate of 2 mV s^{-1}. The durability of HER and OER electrochemical performance were evaluated by time-dependent overpotential curve at a static current density of 100 mA/cm^2. All the LSV curves are corrected with iR compensation.

In Ni_2P-HF || Ni_2P-LF electrolyzer, Ni_2P-HF and Ni_2P-LF (1 cm×1 cm) were employed as anode and cathode materials, respectively. Cu electrode holder was applied to connect the working electrodes, as Cu possesses great electrical conductivety and negligible water splitting performance. LSV curves was also conducted in 1.0 M KOH solution with a scan rate of 5 mV s^{-1} between 1.0 and 1.9 V and the LSV curve was corrected with iR compensation.

Electrochemical active surface area: The active surface area of the prepared samples was estimated by electrochemical capacitance measurements, because the current in non-faradic region is expected to be linearly proportional to the active surface area. The applied potential was set between 0.01 to 0.11 V vs. Hg/HgO for 50 cycles at different scan rates. The capacitive currents were collected at 0.98 V vs RHE. Then, the capacitive currents were plotted as a function of scan rate to calculate the double layer capacitance.

Characterizations: The morphology of SS and SSP samples were characterized by scanning electron microscope, scanning transmission electron microscope (SEM, Jeol JSM-6335F & TEM, Jeol JEM-2100F). The crystal structure and composition were measured by X-ray Diffractometer

(Rigaku SmartLab) and Raman spectroscope (Witec Confocal Raman system) with an excitation wavelength of 532 nm. The electrochemical impedance spectroscopy (EIS) was performed in Solartron Electrochemical workstation (German) with the frequency ranging from 0.01 to 10^5 Hz. The surface valence state of sample was tested by using X-ray photoelectron spectroscopy (XPS, Thermol Scientific Escalab 250Xi, Al Kα radiation).

Theoretical Calculations: Theoretical calculations were performed using density functional theory (DFT) as implemented in the VASP code (5.4.3) with exchange-correlation energy functional, which were modeled by Perdew-Burke-Ernzerhof (PBE) functional.[46] The cut-off energy was set to be 450 eV and all structures were relaxed to an energy convergence of 10^{-4} eV/atom and a force convergence of 0.02 eV/Å, respectively. During the geometrical optimization, a (3 × 2) Ni_2P surface with exposed (1 -1 0) was applied to investigate the adsorption behavior of intermediates (including H_2O, H*, OH*, O* and OOH*) involved in HER and OER process. The k-points was 3 × 3 × 1 in slab optimization and 5 × 5 × 1 in static calculation. The thickness of vacuum in all the models was set to 30 Å to eliminate the interactions between the layers caused by the periodic boundary condition.

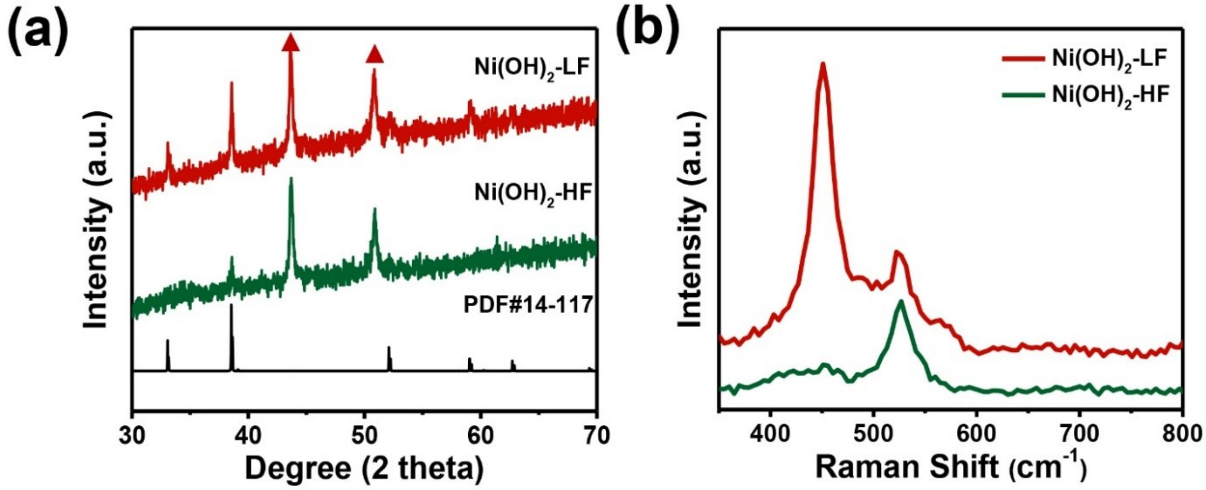

Figure S1. (a) XRD patterns of $Ni(OH)_2$-HF and $Ni(OH)_2$-LF on SS mesh. The typical peak of stainless steel is denoted with red triangle. (b) Raman spectrum of $Ni(OH)_2$-HF and $Ni(OH)_2$-LF collected at low wavenumber.

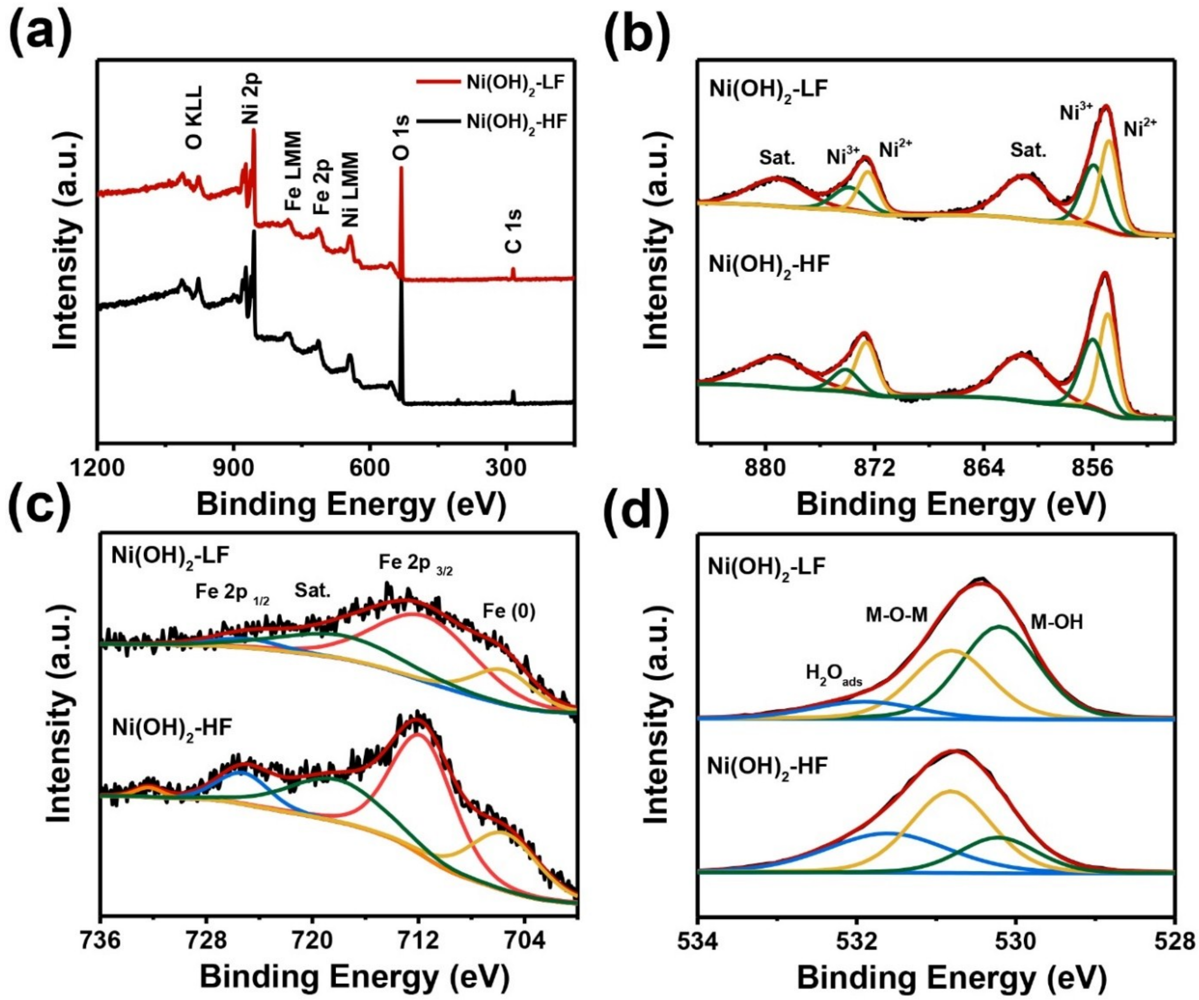

Figure S2. (a) XPS spectra of $Ni(OH)_2$-HF and $Ni(OH)_2$-LF. High resolution XPS spectra of (b) Ni, (c) Fe and (d) O in $Ni(OH)_2$-HF and $Ni(OH)_2$-LF, respectively.

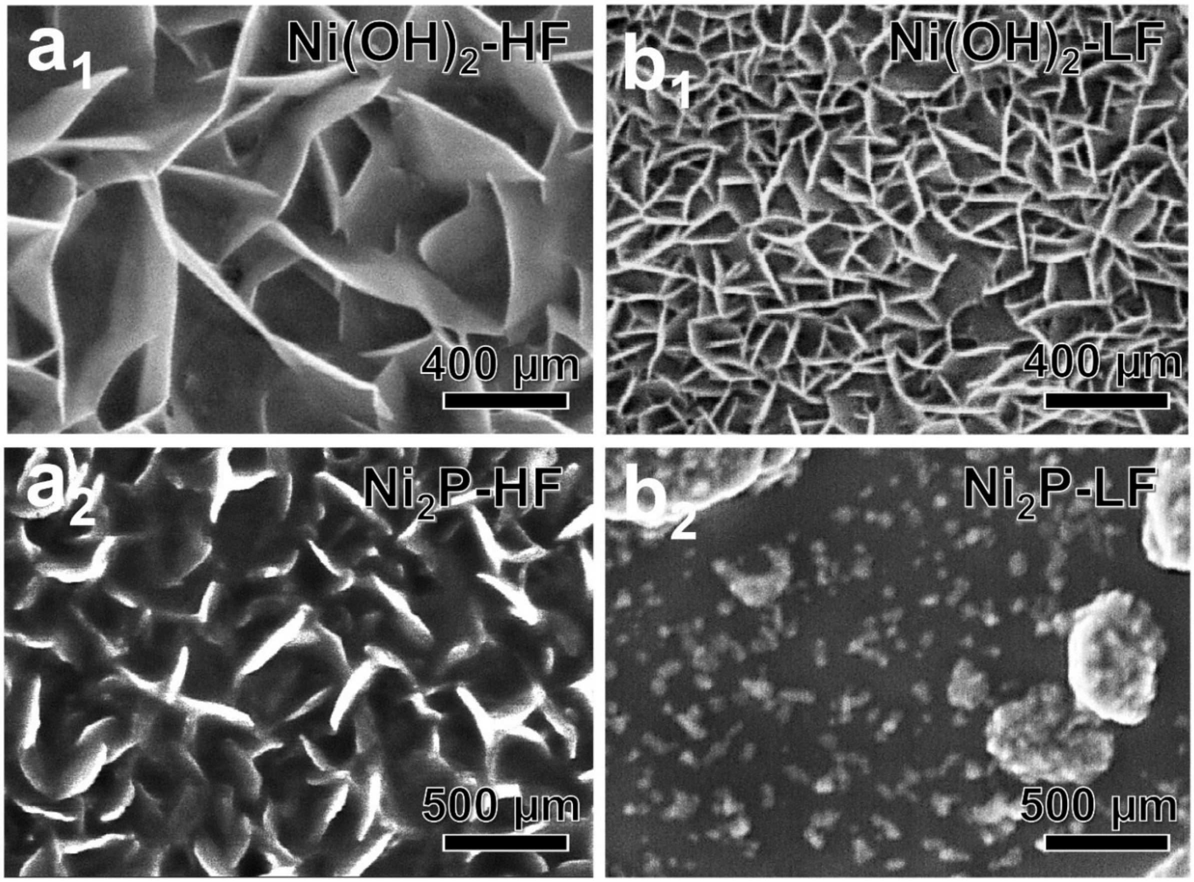

Figure S3. SEM images of (a_1) $Ni(OH)_2$-HF and (b_1) $Ni(OH)_2$-LF on SS mesh, respectively. SEM images of (a_2) Ni_2P-HF and (b_2) Ni_2P-LF, respectively.

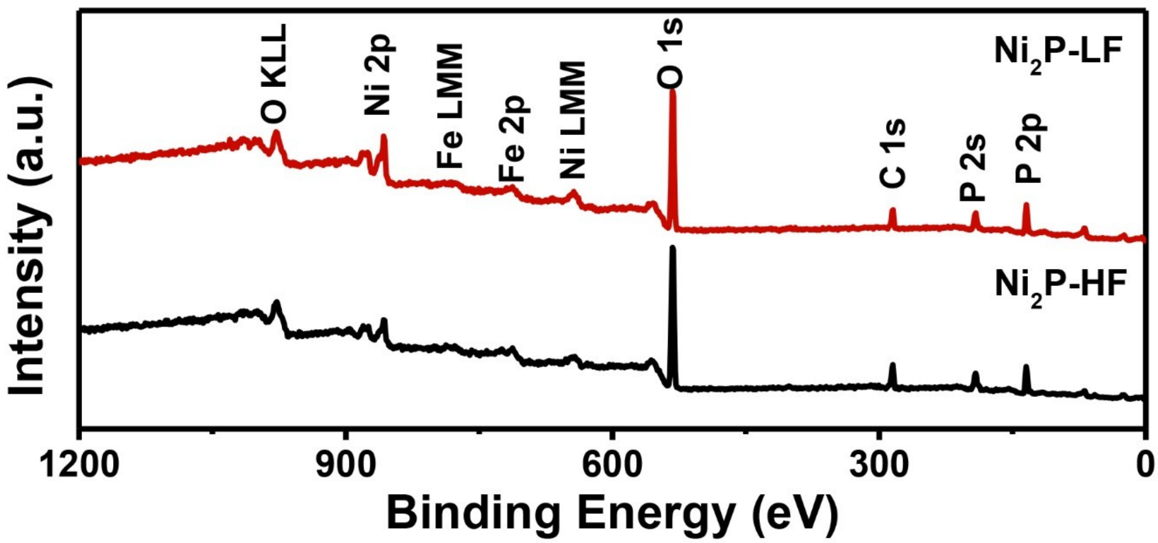

Figure S4. XPS spectra of Ni_2P-HF and Ni_2P-LF, respectively.

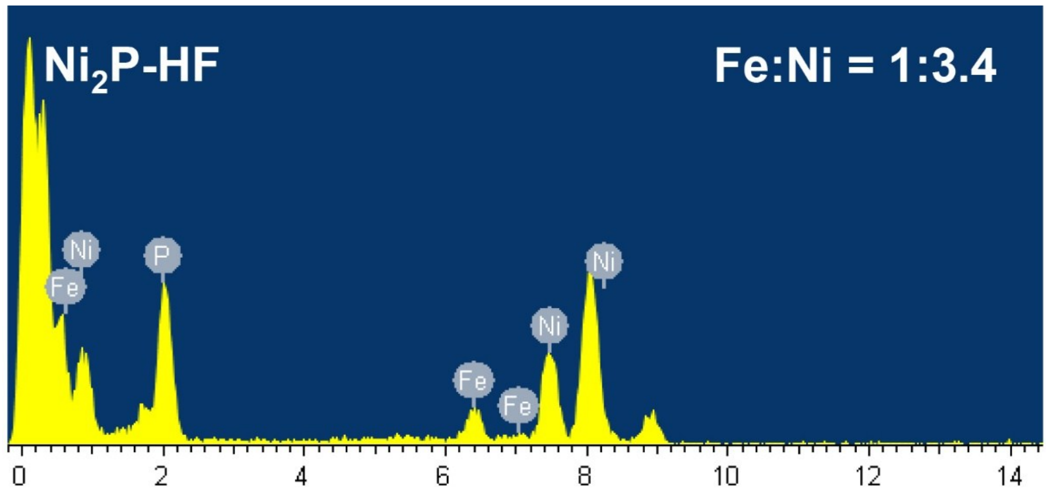

Figure S5. (a) EDX characterization of Ni_2P-HF sample.

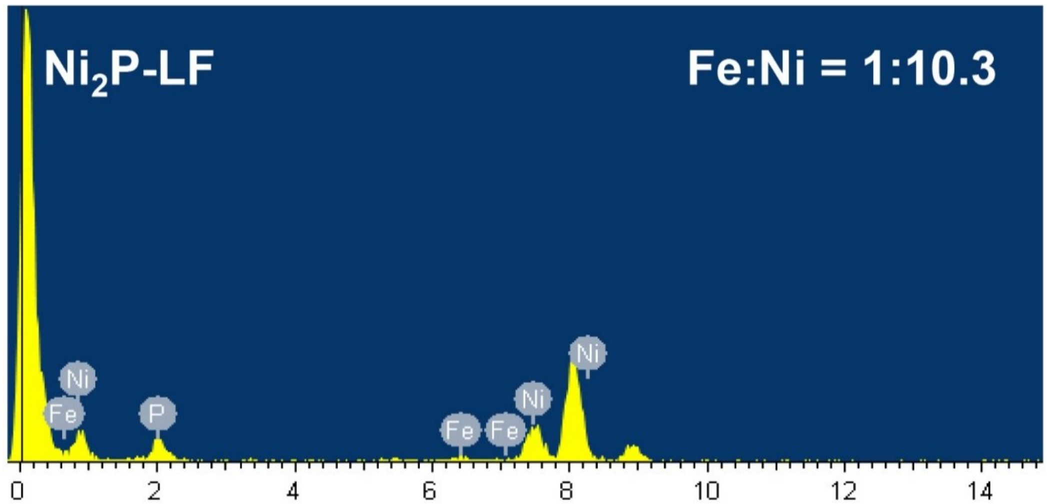

Figure S6. (a) EDX characterization of Ni_2P-LF sample.

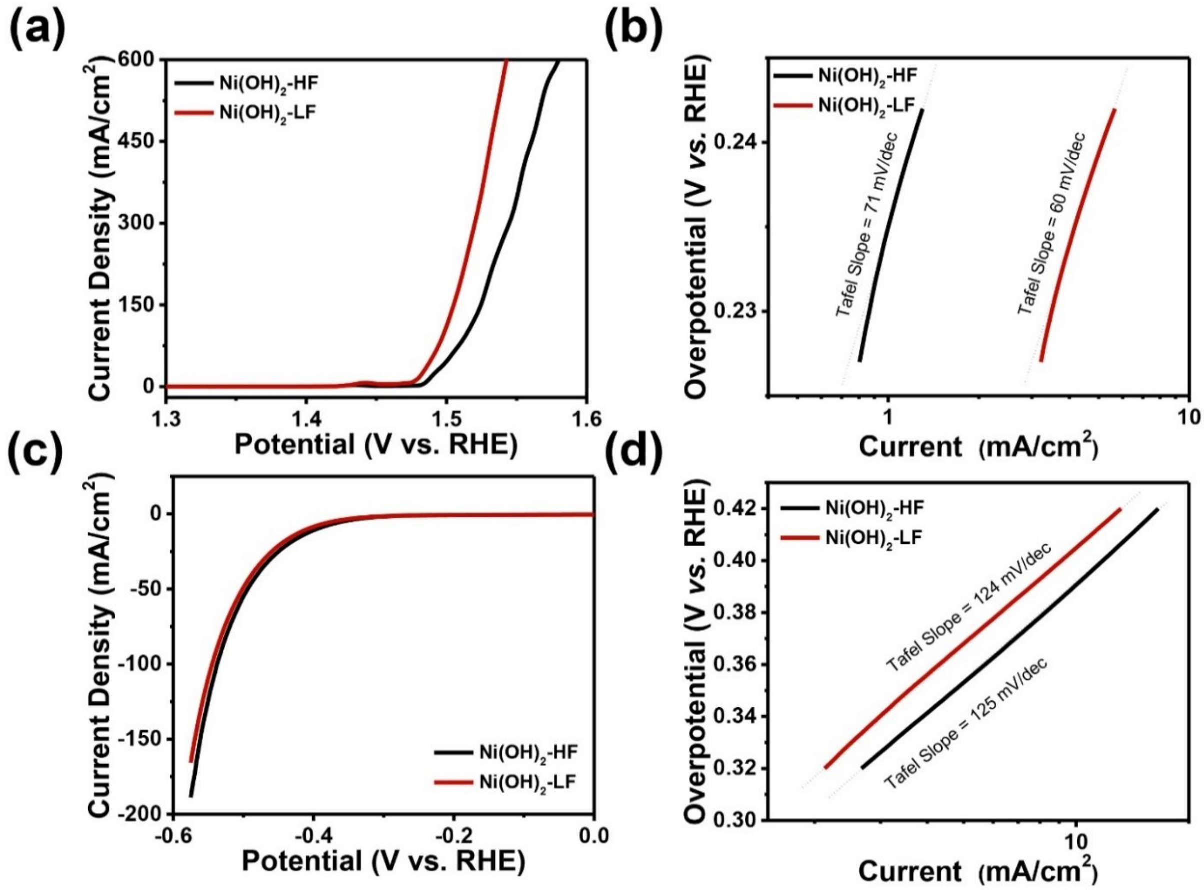

Figure S7. OER performance of $Ni(OH)_2$-HF and $Ni(OH)_2$-LF in 1.0 M KOH. (a) Polarization curves and (b) corresponding Tafel plots after iR compensation. HER performance of $Ni(OH)_2$-HF and $Ni(OH)_2$-LF in 1.0 M KOH. (c) Polarization curves and (d) corresponding Tafel plots after iR compensation.

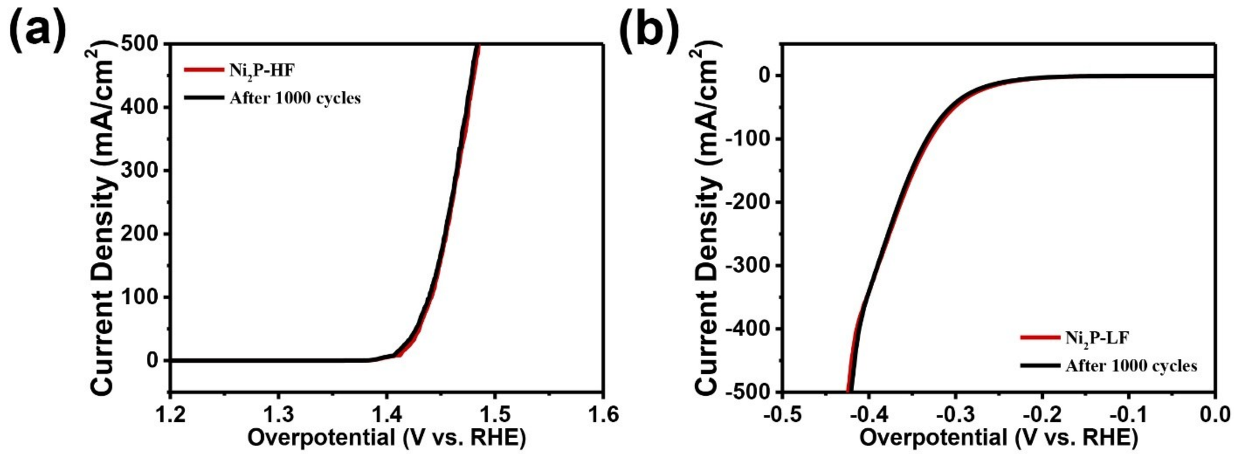

Figure S8. Durability tests of (a) Ni_2P-HF and (b) Ni_2P-LF in 1.0 M KOH.

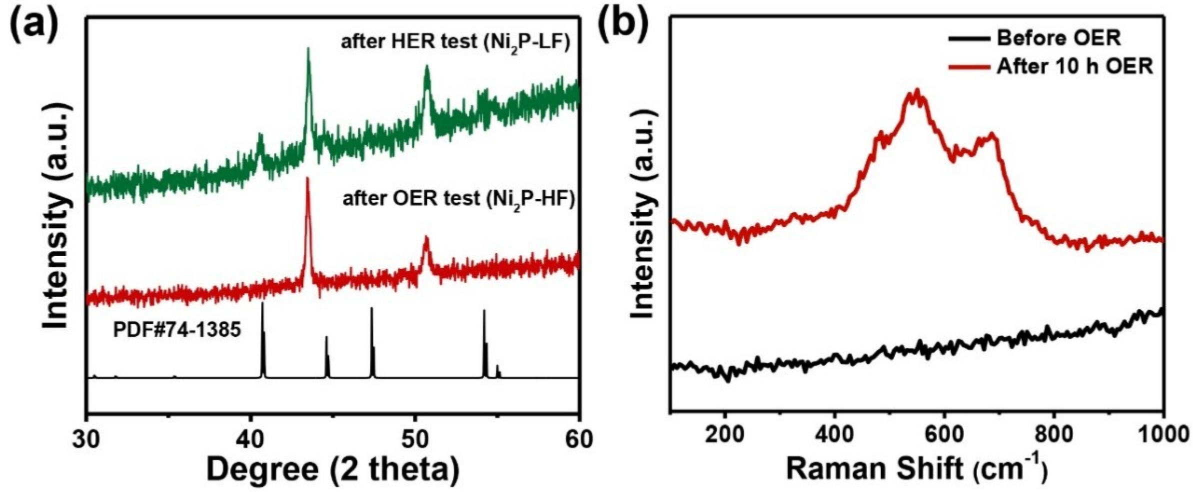

Figure S9. (a) XRD patterns of Ni_2P-HF and Ni_2P-LF after OER and HER test, respectively. (b) Raman spectrum of Ni_2P-HF before and after OER reaction.

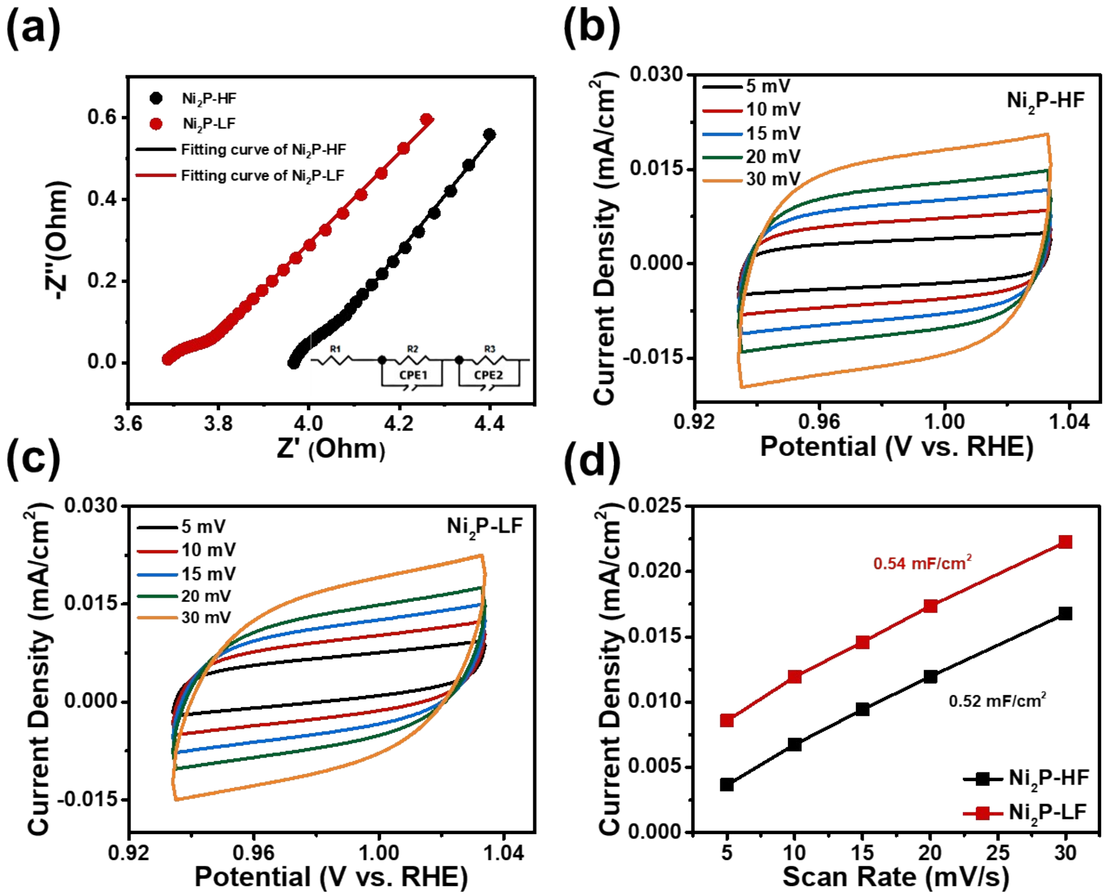

Figure S10. (a) Electrochemical impedance spectroscopy (EIS) Nyquist plots of Ni_2P-HF and Ni_2P-LF, the inset graph shows an electrical equivalent circuit model. Cyclic voltammograms with different scan rates obtained at non-faradaic potential region between 0.01 V and 0.11 V (*vs.* Hg/HgO) of (b) Ni_2P-HF and (c) Ni_2P-LF. (d) The differences in current density at 0.98 V vs RHE plotted as a function of scan rate, the slope of fitting line represents active electrochemical area of electrocatalyst.

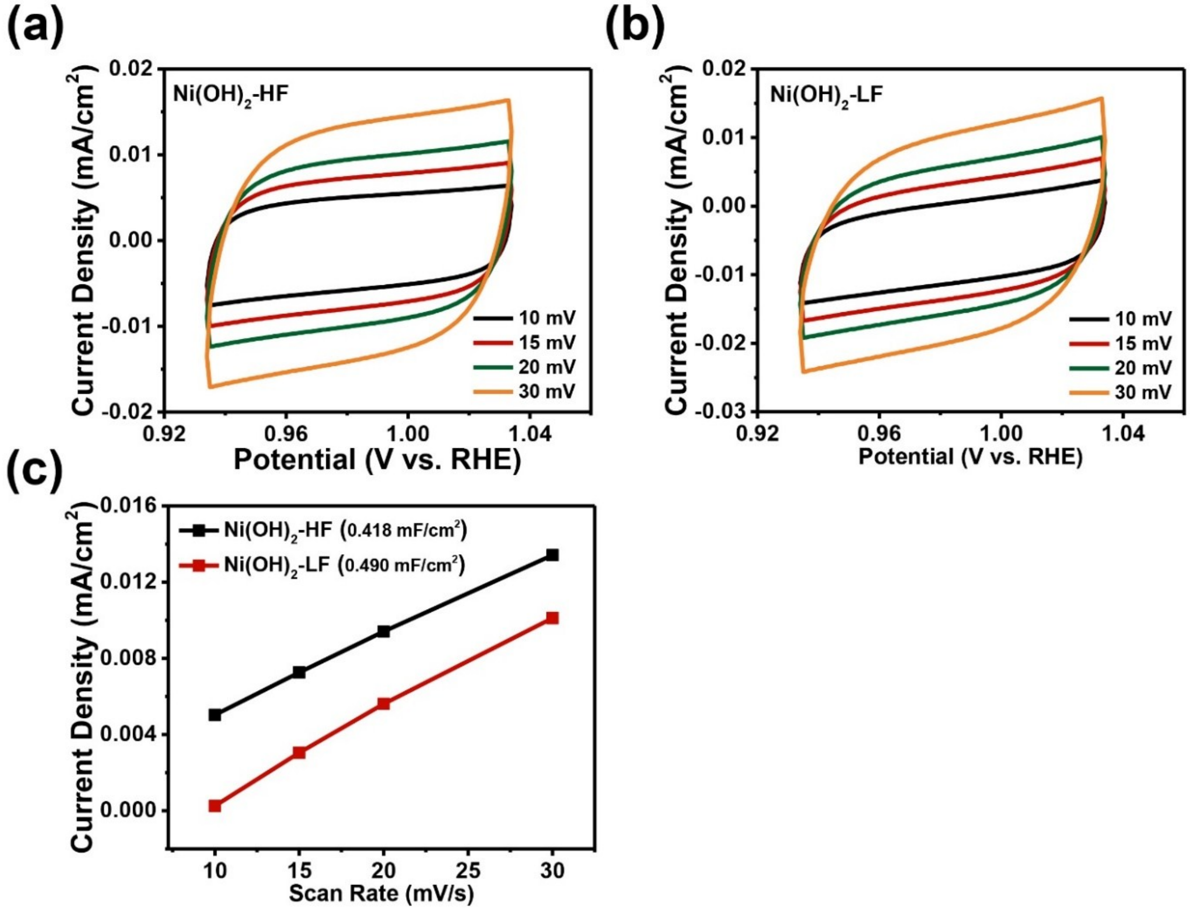

Figure S11. Cyclic voltammograms obtained at non-faradaic potential region between 0.01 V and 0.11 V (vs. Hg/HgO) of (a) $Ni(OH)_2$-HF and (b) $Ni(OH)_2$-LF samples, respectively. (c) The differences in current density at 0.98 V vs RHE plotted as a function of scan rate, the slope of fitting line represents active electrochemical area of electrocatalyst.

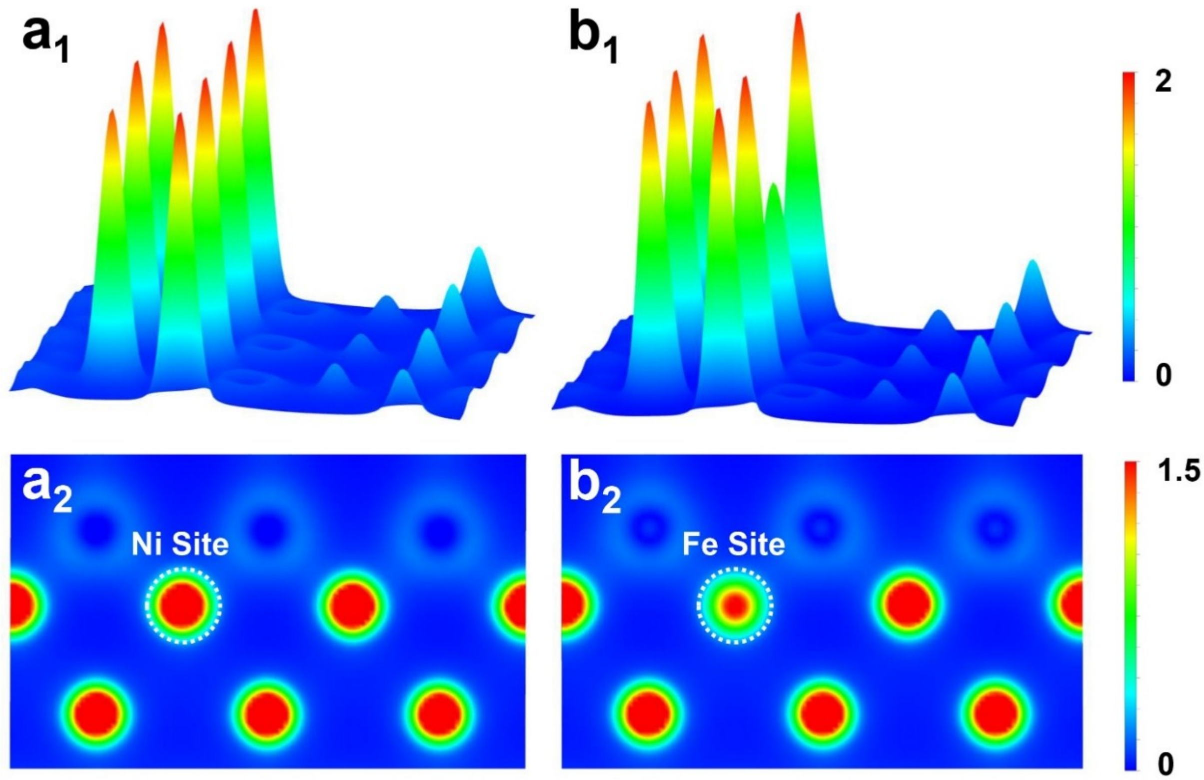

Figure S12. Electron density contour maps for Ni_2P surface (a_1-a_2) without and (b_1-b_2) with Fe dopant. (a_1) and (b_1) are bird's-eye view.

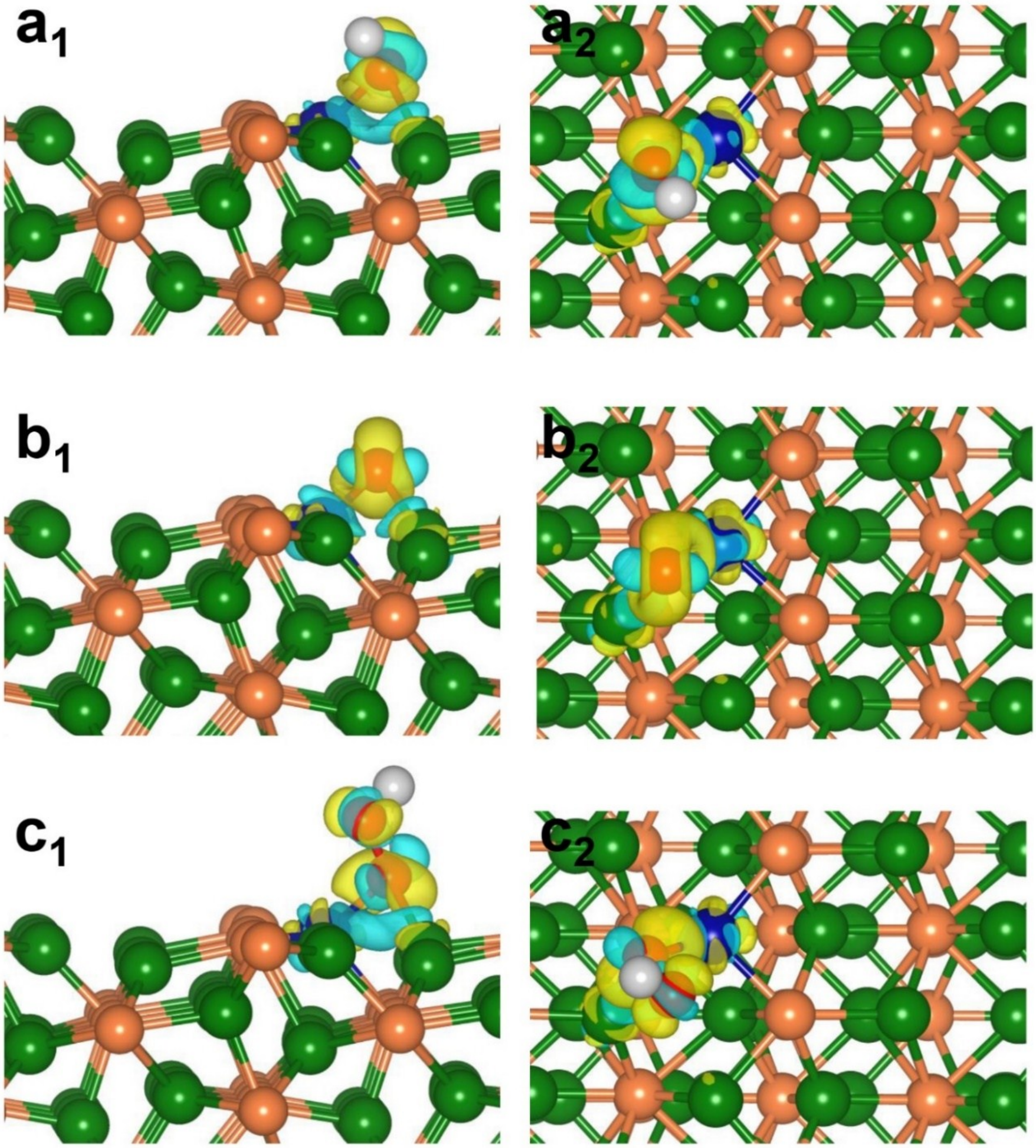

Figure S13. (a_1) Side view and (a_2) top view of the charge density difference of the OH*-adsorbed on Fe-doped Ni_2P surface. (b_1) Side view and (b_2) top view of the charge density difference of the O*-adsorbed on Fe-doped Ni_2P surface. (c_1) Side view and (c_2) top view of the charge density difference of the OOH*-adsorbed on Fe-doped Ni_2P surface. The yellow and blue isosurfaces represent charge accumulation and depletion, respectively. The isovalue is 0.005 au. For clarity, the symmetric parts of the optimized slabs at the bottom are not shown.

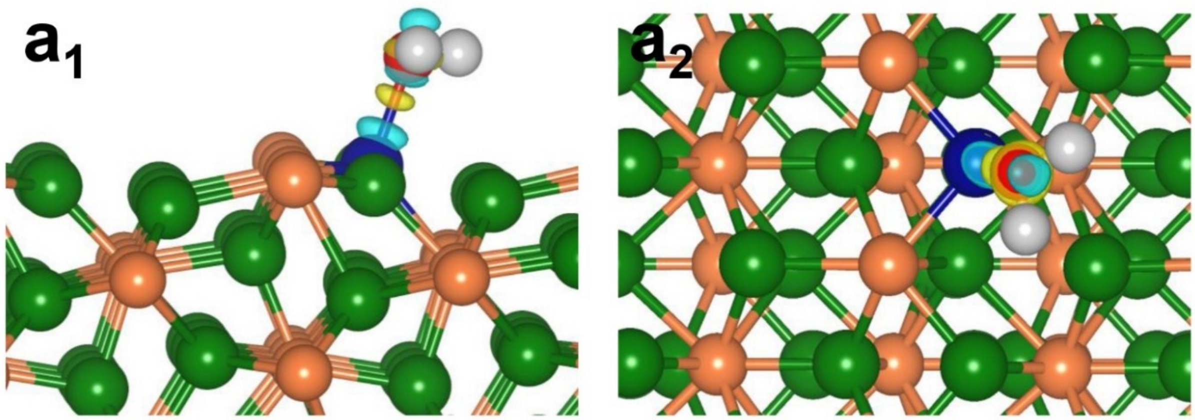

Figure S14. (a_1) Side view and (a_2) top view of the charge density difference of the H_2O-adsorbed on Fe-doped Ni_2P surface. The yellow and blue isosurfaces represent charge accumulation and depletion, respectively. The isovalue is 0.005 au. For clarity, the symmetric parts of the optimized slabs at the bottom are not shown.

Table S1. Elemental composition analysis of Ni_2P-HF and Ni_2P-LF.

	Content of Fe	Content of Ni	Content of P
Ni_2P-HF	7.51%	22.46%	70.03%
Ni_2P-LF	3.37%	34.46%	62.17%

Table S2. Comparison of OER performance of self-supported Fe-doped Nickel Phosphides.

	Overpotential for OER	Tafel Slope	References
$Ni_{1.85}Fe_{0.15}P$/Ni foam	380 mV @ 200 mA/cm^2	96 mV/dec	Wang Pengyan et al.[1]
NiFe-OH/NiFeP/Ni foam	255 mV @ 300 mA/cm^2	39 mV/dec	Liang Hanfeng et al.[2]
Amorphous Metallic NiFeP	390 mV @ 400 mA/cm^2	42 mV/dec	Hu Fei et al.[3]
Fe-doped Ni_2P/Carbon cloth	310 mV @ 300 mA/cm^2	48 mV/dec	Wang Jianmei et al.[4]
$(Fe_{0.5}Ni_{0.5})_2P$/Ni foam	260 mV @ 500 mA/cm^2	66 mV/dec	Zhang Bowei et al.[5]
$Fe(PO_3)_2/Ni_2P$ /Ni foam	265 mV @ 500 mA/cm^2	51.9 mV/dec	Zhou Haiqing et al.[6]
FeNiP/Ni foam	240 mV @ 60 mA/cm^2	76 mV/dec	Manman Qian et al.[7]
Fe-doped Ni_2P/SS	**255 mV @ 500 mA/cm^2**	**29.1 mV/dec**	**This work**

Table S3. Comparison of overpotentials for HER and OER reactions.

	Overpotential for HER	**Overpotential for OER**	**References**
NiP/Ni foam	185 mV @ 60 mA/cm^2	320 mV @ 100 mA/cm^2	Chen Gaofeng et al.[8]
Fe-doped Ni_2P/Ni foam	310 mV @ 200 mA/cm^2	260 mV @ 300 mA/cm^2	Li Yingjie et al.[9]
N- and P-doped SS	> 400 mV @ 100 mA/cm^2	> 600 mV @ 100 mA/cm^2	Balogun Muhammad-Sadeeq et al.[10]
Fe/Ni Phosphides on Ni foam	230 mV @ 400 mA/cm^2	290 mV @ 400 mA/cm^2	Xiao Chunhui et al.[11]
N-doped Ni_3S_2/Ni foam	250 mV @ 160 mA/cm^2	380 mV @ 400 mA/cm^2	Chen Pengzuo et al.[12]
NiFe LDH/Cu foam	192 mV @ 100 mA/cm^2	311 mV @ 500 mA/cm^2	Yu Luo et al.[13]
MoO_x/Ni_3S_2/Ni	480 mV @ 500 mA/cm^2	520 mV @ 500 mA/cm^2	Wu Yuanyuan et al.[14]
Co–Mn carbonate hydroxide/Ni foam	450 mV @ 500 mA/cm^2	400 mV @ 500 mA/cm^2	Tang Tang et al.[15]
Fe-doped Ni_2P/SS	**400 mV @ 500 mA/cm^2**	**255 mV @ 500 mA/cm^2**	**This work**

Table S4. Comparison of potentials for overall water splitting in two-electrode system.

	Potential	**References**
$Ni_{1.85}Fe_{0.15}P$/Ni foam || $Ni_{1.85}Fe_{0.15}P$/Ni foam	1.87 V @ 100 mA/cm^2	Wang Pengyan et al.[1]
IrO_2/Ni foam || Pt-C/Ni foam	1.77 V @ 100 mA/cm^2	
Ni_2P/Ni foam || Ni_2P/Ni foam	1.82 V @ 100 mA/cm^2	Menezes Prashanth W. et al.[16]
Co_3Se_4/Co foam || Co_3Se_4/Co foam	1.88 V @ 100 mA/cm^2	Li Wei et al.[17]
RuO_2/Co foam || Pt-C/Co foam	1.90 V @ 100 mA/cm^2	
NiP /Ni foam || NiP/Ni foam	1.80 V @ 40 m A/cm^2	Chen Gaofeng et al.[8]
$(Ni_{0.33}Fe_{0.67})_2P$/Ni foam || $(Ni_{0.33}Fe_{0.67})_2P$/Ni foam	1.73 V @ 100 mA/cm^2	Li Yingjie et al.[9]
$FeNiP_x$/Ni foam || $FeNiP_x$/Ni foam	1.85 V @ 100 mA/cm^2	Xiao Chunhui et al.[11]
NiCoP/Ni foam || NiCoP/Ni foam	1.83 V @ 100 mA/cm^2	Liang Hanfeng et al.[2]
N-Ni_3S_2/Ni foam || N-Ni_3S_2/Ni foam	1.82 V@ 100 mA/cm^2	Chen Pengzuo et al.[12]
Fe-doped Ni_2P (1h)/SS || Fe-doped Ni_2P (3h)/SS	**1.80 V @ 100 mA/cm^2**	**This work**

Reference

[1] P. Wang, Z. Pu, Y. Li, L. Wu, Z. Tu, M. Jiang, Z. Kou, I. S. Amiinu, S. Mu, *ACS Appl. Mater. Inter.* **2017**, *9*, 26001.

[2] H. Liang, A. N. Gandi, C. Xia, M. N. Hedhili, D. H. Anjum, U. Schwingenschlögl, H. N. Alshareef, *ACS Energy Lett.* **2017**, *2*, 1035.

[3] F. Hu, S. Zhu, S. Chen, Y. Li, L. Ma, T. Wu, Y. Zhang, C. Wang, C. Liu, X. Yang, L. Song, X. Yang, Y. Xiong, *Adv. Mater.* **2017**, *29*, 1606570.

[4] J. Wang, X. Ma, F. Qu, A. M. Asiri, X. Sun, *Inorg. Chem.* **2017**, *56*, 1041.

[5] B. Zhang, Y. H. Lui, H. Ni, S. Hu, *Nano Energy* **2017**, *38*, 553.

[6] H. Zhou, F. Yu, J. Sun, R. He, S. Chen, C.-W. Chu, Z. Ren, *Proc. Natl. Acad. Sci. USA* **2017**, *114*, 5607.

[7] M. Qian, S. Cui, D. Jiang, L. Zhang, P. Du, *Adv. Mater.* **2017**, *29*, 1704075

[8] G.-F. Chen, T. Y. Ma, Z.-Q. Liu, N. Li, Y.-Z. Su, K. Davey, S.-Z. Qiao, *Adv. Funct. Mater.* **2016**, *26*, 3314.

[9] Y. Li, H. Zhang, M. Jiang, Q. Zhang, P. He, X. Sun, *Adv. Funct. Mater.* **2017**, *27*, 1702513.

[10] M. S. Balogun, W. Qiu, Y. Huang, H. Yang, R. Xu, W. Zhao, G. R. Li, H. Ji, Y. Tong, *Adv. Mater.* **2017**, *29*, 1702095.

[11] C. Xiao, B. Zhang, D. Li, *Electrochim. Acta* **2017**, *242*, 260.

[12] P. Chen, T. Zhou, M. Zhang, Y. Tong, C. Zhong, N. Zhang, L. Zhang, C. Wu, Y. Xie, *Adv. Mater.* **2017**, *29*, 1701584.

[13] L. Yu, H. Zhou, J. Sun, F. Qin, F. Yu, J. Bao, Y. Yu, S. Chen, Z. Ren, *Energ. Environ. Sci.* **2017**, *10*, 1820.

[14] Y. Wu, G.-D. Li, Y. Liu, L. Yang, X. Lian, T. Asefa, X. Zou, *Adv. Funct. Mater.* **2016**, *26*, 4839.

[15] T. Tang, W. J. Jiang, S. Niu, N. Liu, H. Luo, Y. Y. Chen, S. F. Jin, F. Gao, L. J. Wan, J. S. Hu, *J. Am. Chem. Soc.* **2017**, *139*, 8320.

[16] P. W. Menezes, A. Indra, C. Das, C. Walter, C. Göbel, V. Gutkin, D. Schmeiβer, M. Driess, *ACS Catal.* **2016**, *7*, 103.

[17] W. Li, X. Gao, D. Xiong, F. Wei, W.-G. Song, J. Xu, L. Liu, *Adv. Energy Mater.* **2017**, *7*, 1602579.